Supplementary Information

Real-time Optical Detection of Single Human and Bacterial Viruses Based on Dark-field Interferometry

1 Experimental Set-up

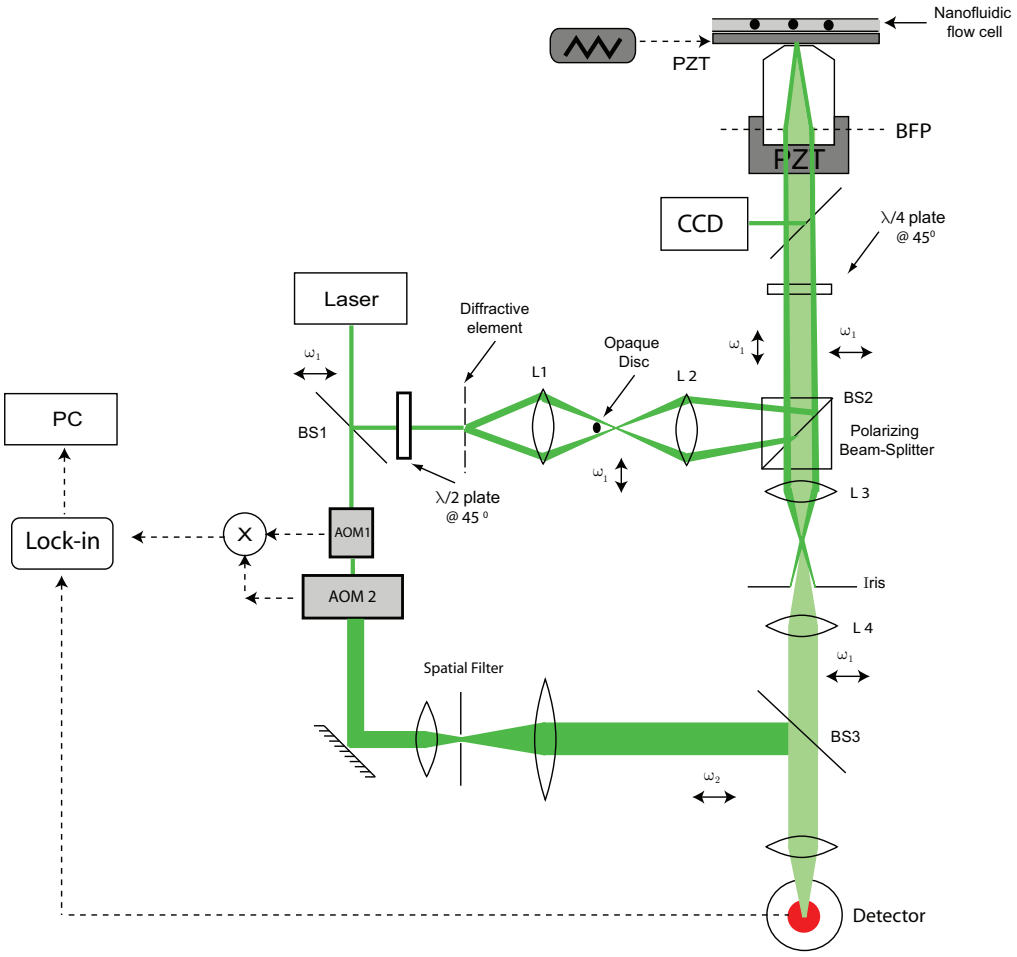

Figure 1: *Detailed schematic for the experimental set-up used for dark-field interferometric detection.*

Fig. 1 shows a schematic of the dark-field interferometric detection system. A p-polarized $\lambda = 532$ nm CW laser beam is first split into two paths by a 90/10 beam-splitter (BS1). The light transmitted by the beam splitter forms the reference arm of the interferometer, and the reflected beam forms the excitation path. The polarization of the reflected beam is converted to vertical using a half-waveplate. By means of a diffractive optical element made of a binary surface with a radial phase grating [2] the beam is then converted to an expanding annulus. Lens L1 forms an image of the annulus at its focal plane, after which the annulus is imaged onto the back-focal plane (BFP) of a high-NA objective by lens L2, and is brought to a focus at the sample plane (the nanofluidic flow-cell) above the objective. An opaque disk (a silver dot on a glass cover-slip) is placed at the focal plane of lens L1 to remove residual traces of zeroth order illumination from the diffractive element. Note that upon incidence on the polarizing beam-splitter BS2, the vertically polarized beam is completely reflected towards the objective without loss of power.

A single nanochannel in the nanofluidic flow-cell is first positioned in the laser focus using a piezoelectric translation system. The sample solution containing nanoparticles such as viruses is introduced into one of the reservoirs of the flow-cell, and flow is induced by use of a pressure-driven flow mechanism (See Methods in main paper for description of nanofluidic flow-cells and flow mechanisms). The light scattered from individual nanoparticles traversing the laser focus is collected by the same objective and is directed through a beam-splitter BS2 to lens L3. A quarter-wave plate (with fast axis at 45°) in front of the objective circularly polarizes the incident light, but then converts the polarization of the scattered light into horizontal. Thus, the scattered light is completely transmitted by BS2 without loss of power. An annular disk (an iris) is placed at the focal plane of lens L3 (which is conjugate to the objective's BFP) to block the light reflected from the glass-water interfaces in the nanochannel. The scattered light from the particles (shown with a lighter shade of green in Fig. 1), passes through the annular disk unperturbed and is collimated by lens L4 and directed to a 50/50 beam-splitter BS3.

The reference beam is frequency-shifted (by $\Delta\omega$) by a pair of acousto-optic modulators and recombined with the scattered light by beam-splitter BS3. Both the reference beam and the scattered beam are spatially filtered (for simplicity, the spatial filter for the scattered

beam is not shown in Fig. 1) to flatten their respective phase fronts. The two beams are then combined and projected on the detector surface. The detector signal is processed by a lock-in amplifier using the reference frequency $\Delta\omega$, and is acquired in real-time.

2 Estimation of illumination spot size in dark-field interferometric detection

In the following we estimate the size of the focal illumination spot that we have in the dark-field detection technique. The output of our laser $\lambda = 532$ nm has a beam diameter of 0.3 mm. This is the beam waist w_0 for the beam incident on the diffractive optical element (DOE, c.f. Fig.1 above). This beam is diffracted from the DOE and focused by lens L1 ($f1 = 4.03$ mm) so that the first order diffracted beam from the DOE forms an annular ring at the focus plane of L1. The width w_1 of the ring is the diffraction limit of the incident gaussian beam on the DOE, and can be determined to be([2])

$$w_1 = \frac{\lambda\, f1}{\pi\, w_0} = 2.27\ \mu\ m. \tag{1}$$

Now the annulus is imaged to the back-focal plane of our objective lens by lens L2 ($f2 = 100$ mm). Lens L2 is $u = 116$ mm away from the focal plane of L1, and the location of the back-focal plane of the objective lens is $v = 725$ mm from lens L2. So, the magnification of the image of the annulus at the objective back-focal plane would be $M = \frac{v}{u} = 6.25$, and its width would be $w_2 = M \times w_1 = 14.2\,\mu$m. The focal length of the microscope objective can be determined from its back-aperture size and NA to be $f3 = 1.53$ mm. Hence the illumination spot at the objective front-focal plane (the sample plane) would be

$$w_3 = \frac{\lambda\, f3}{\pi\, w_2} = 18.2\ \mu\ m. \tag{2}$$

Hence we can see that the illumination spot at the sample plane can be estimated to be $\sim 18\mu$m in size, as mentioned in Section 2 of the paper. Fig. 2 illustrates the illumination spot sizes for illumination with a tightly focused laser beam and for dark-field detection. One can see that the illumination is essentially uniform across the nanochannel in the

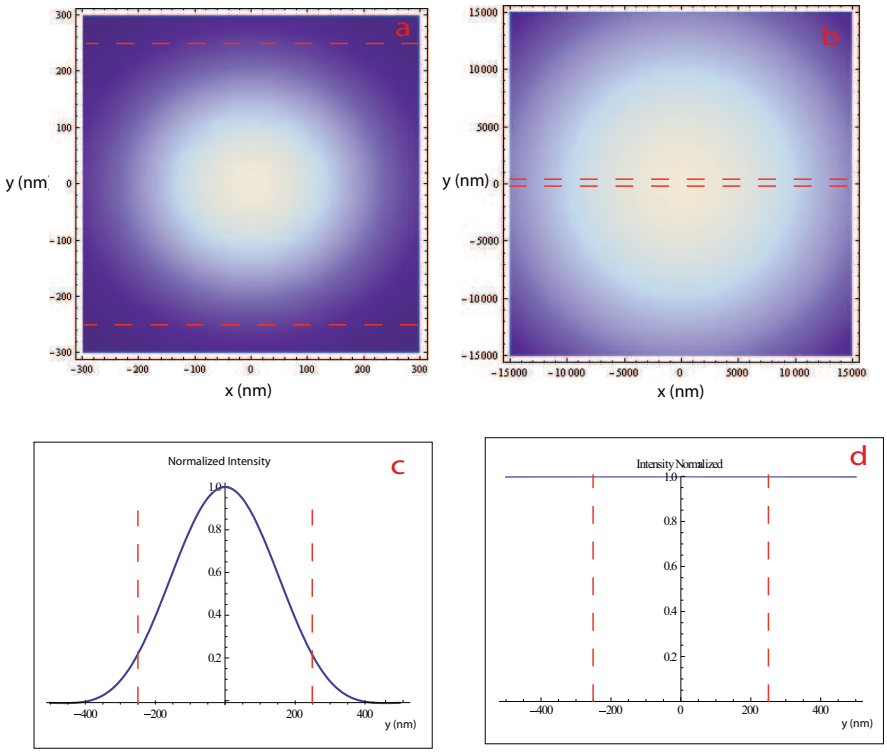

Figure 2: *Illumination spot size and its effect on particle size resolution. (***a***) Density plot for illumination spot in the x-y plane (x being the direction of particle flow) for a tightly focused laser beam, such as the one used in [1]. The yellow dashed lines outline the dimensions of a nanochannel. (***b***) Density plot for illumination spot in case of the illumination in the dark field approach.. Note that the focus intensity variation across a nanochannel is negligible in this case. (***c***and* **d***) Normalized intensity distribution in the lateral (y) direction with red dashed lines showing the extent of a nanochannel. This graphic explains the improvement in size resolution for dark-field detection (c.f. Fig.3 in main paper).*

dark-field configuration. This clearly shows, that in the dark-field case, trajectory variation of the particles traversing a nanofluidic channel has a negligible contribution to the width of the size distribution for an ensemble of particles, as observed experimentally (c.f. Fig. 4 below).

3 Lowering of detection noise floor in Dark-field Interferometric detection

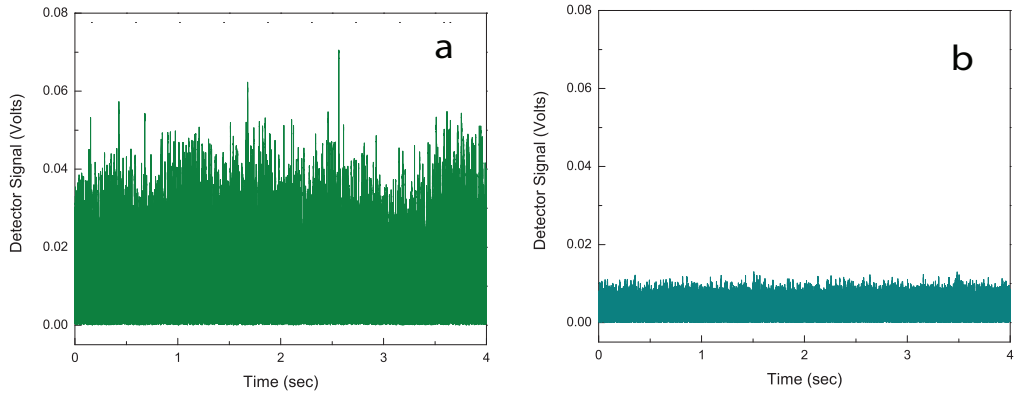

Figure 3: *Noise-reduction by dark-field interferometric detection.(***a***) Detector noise before elimination of background light. Note the variations in the noise amplitude due to instabilities in the interferometer.(***b***) Detector noise after elimination of background light with dark-field detection. Note that the only contribution to the noise floor is shot noise due to the reference field.(a) and (b) have been recorded for the same laser power in the nanochannel.*

In this Section we experimentally demonstrate the improvement in signal-to-noise ratio (SNR) achieved with darkfield detection. Fig. 3a shows acquired detector signal in a bright-field configuration, when the incident beam is tightly focused into a nanofluidic channel filled with bare TNE buffer(0.01 M Tris pH 7.2, 0.1 M NaCl, 1 mM EDTA), and the backreflected light $\mathbf{E}_{\mathrm{b}}$ interferes with the reference field $\mathbf{E}_{\mathrm{r}}$ on a split photodetector. The low-frequency variations in the noise amplitude are due to the beam pointing instabilities in the interferometer. Fig. 3b shows the detector signal acquired in the dark-field configuration, using the same laser power in the nanochannel as in the previous case. The low-frequency variations are now eliminated and the noise amplitude is ~ 5 times lower than in the bright-field case. Since the backreflected light $\mathbf{E}_{\mathrm{b}}$ is blocked, it no longer contributes to the noise floor. The remaining noise is mainly shot noise from the reference field. The reduction in noise floor makes it possible to detect small bioparticles, such as bacteriophage and larger proteins.

4 Comparison of size distributions between dark-field interferometric detection and a bright-field technique

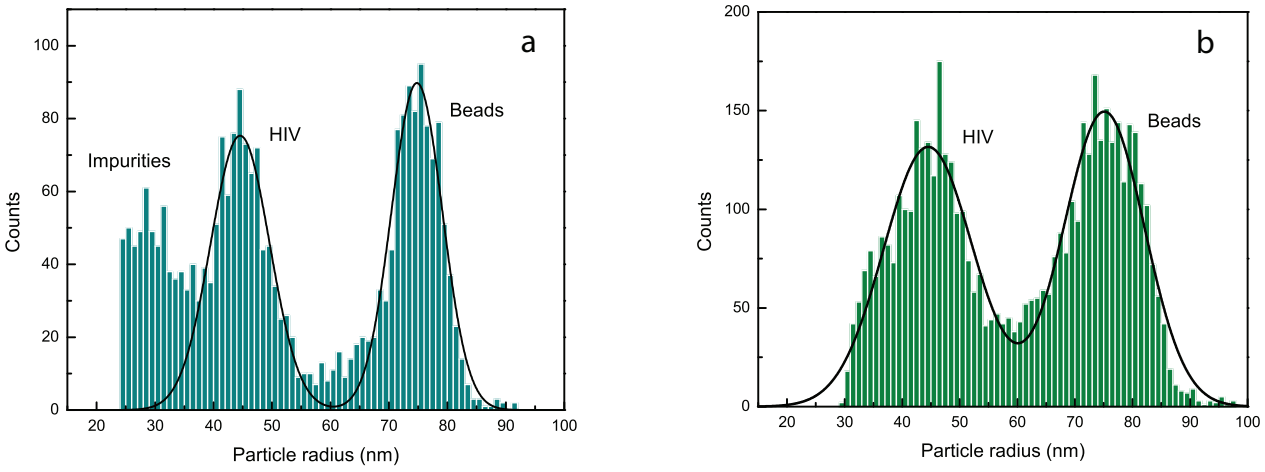

Figure 4: *Comparison of the size distribution of a sample containing HIV AT2WT wild-type virus in cell media mixed with 75 nm polystyrene beads, obtained using the (***a***) current dark-field interferometric technique (same as Fig.2a in the main paper), and (***b***) a bright-field interferometric technique [1] which does not eliminate background light. Note that the sample appears pure in (b), but is shown to have impurities when using the dark-field method. Also note the narrower distributions and hence better size-resolution in (a).*

Here we show experimentally how the sensitivity and resolution of our dark-field interferometric measurements compare with that using a bright-field configuration, such as that described in [1]. Fig. 4 compares the size distributions obtained for the HIV AT2WT wild-type virus in cell culture media (c.f. Fig. 3 in the main paper) using the current dark-field configuration and the configuration described in [1]. A comparison between Fig. 4a and 4b clearly establishes two distinct advantages of the dark-field method. Firstly, the current technique enables us to detect small nano-size impurities in the sample (such as exosomes or partially formed viral capsids), which are not detectable with the bright-field scheme. This corroborates our expectation that dark-field detection enables higher detection sensitivity. Secondly, the individual size distributions of the virus and polystyrene beads are narrower in Fig. 4a and 4b, which again is what we expect due to the negli-

gible variation of excitation intensity across a nanofluidic channel with dark-field illumination when compared with bright-field illumination (c.f. Fig.2 above). The current darkfield method (Fig. 4a) yields $\sigma = 5.05$ nm and $\sigma = 4.36$ nm for the standard deviations (SD) of the HIV and polystyrene particle distributions. On the other hand, the bright-field method (Fig. 4b) yields $\sigma = 7.74$ nm and $\sigma = 6.98$ nm respectively. The SD of the polystyrene beads size distribution obtained with the current method matches the manufacturer specifications better.

5 TEM images for HIV virus

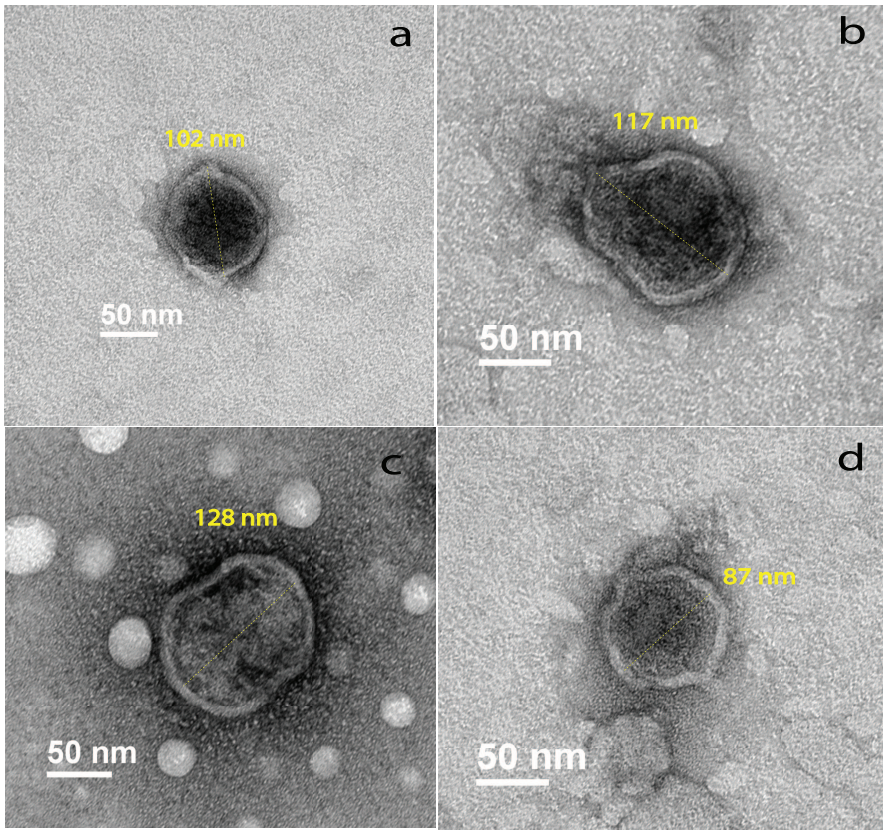

Figure 5: *TEM images for different individual HIV virus particles in the HIV ADA strain sample used to obtain results shown in Fig.3 and Fig.4 in the main paper.*

6 TEM images for phage

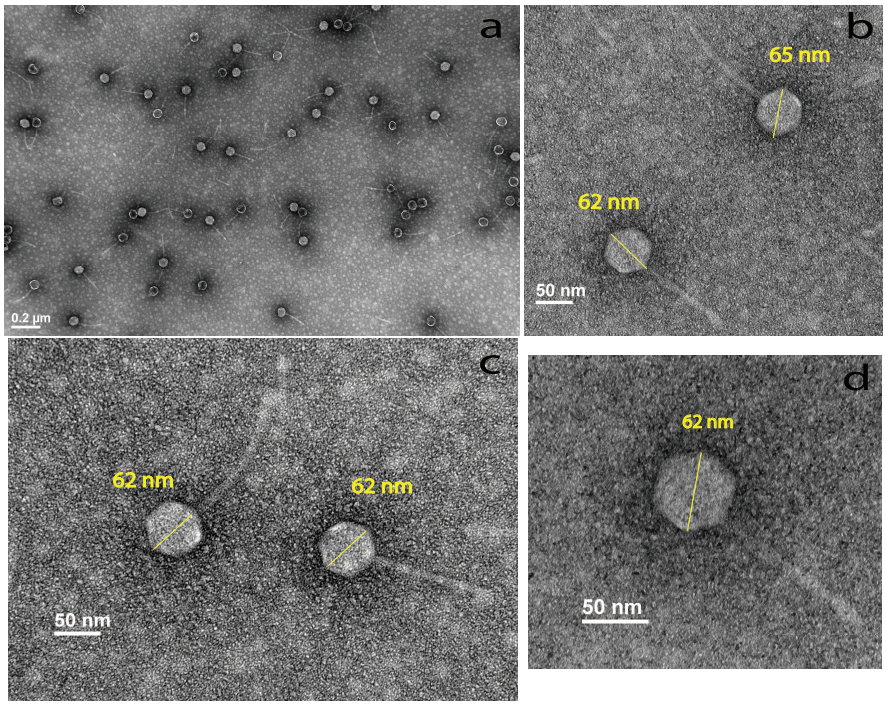

Figure 6: *TEM images for different individual phage particles in the sample used to obtain results shown in Fig.4 in the main paper. We observed that the size distribution in TEM images is narrower for phage than for HIV virus, which supports the observation from the optical size measurements.*

References

[1] Mitra, A., Deutsch, B., Ignatovich, F., Dykes, C., and Novotny, L. Nano-optofluidic detection of single viruses and nanoparticles. *ACS Nano* **4**, 1305–1312 (2010).

[2] Ozeri, R.,Khaykovich, L., Friedman, N., and Davidson, N. Large-volume single-beam dark optical trap for atoms using binary phase elements. *J. Opt. Soc. Am. B* **17**, 1113–1116 (2000).